

Influence of stress relief heat treatment on the residual stress state of a L-PBF AlSi10Mg alloy

Ilaria Roveda^{1*}, Itziar Serrano-Munoz^{1*}, Tatiana Mishurova¹, Mauro Madia¹, Thilo Pirling², Alexander Evans¹, Manuela Klaus³, Jan Haubrich⁴, Guillermo Requena^{4,5}, Giovanni Bruno^{1,6}

¹ *Bundesanstalt für Materialforschung und –prüfung (BAM), Unter den Eichen 87, 12205 Berlin, Germany*

² *Institut Laue-Langevin, 71 avenue des Martyrs, CS 20156, 38042 Grenoble cedex 9, France*

³ *Helmholtz-Zentrum Berlin für Materialien und Energie GmbH, Hahn-Meitner Platz 1, Berlin 14109, Germany*

⁴ *Institute of Materials Research, German Aerospace Center (DLR), Linder Höhe, 51147 Cologne, Germany*

⁵ *Metallic Structures and Materials Systems for Aerospace Engineering, RWTH Aachen University, 52062 Aachen, Germany*

⁶ *Institute of Physics and Astronomy, University of Potsdam, Karl-Liebknecht-Str.24-25, 14476 Potsdam, Germany*

<https://doi.org/10.1016/j.ijfatigue.2023.107808>

*Corresponding author: ilaria.roveda@bam.de; itziar.serrano-munoz@bam.de

Abstract

Laser Powder Bed Fusion (L-PBF) additive manufacturing (AM) induces high magnitude residual stress (RS) in structures due to the extremely heterogeneous cooling and heating rates. As the RS can be deleterious to the fatigue resistance of engineering components, great efforts are focused on understanding their generation and evolution after post-process heat treatments. In this study, the RS relaxation induced in an as-built L-PBF AlSi10Mg material by a low-temperature annealing heat treatment (265 °C for 1 hour) is studied by means of X-ray and neutron diffraction. Since the specimens are manufactured using a baseplate heated up to 200 °C, low RS are found in the as-built condition. After heat treatment a redistribution of the RS is observed, while their magnitude remains constant. It is proposed that the redistribution is induced by a repartition of stresses between the α -aluminium matrix and the silicon phase, as the morphology of the silicon phase is affected by the heat treatment. A considerable scatter is observed in the neutron diffraction RS profiles, which is principally correlated to the presence (or absence) of *pockets* of porosity developed at the borders of the chessboard pattern.

Key words: Additive manufacturing (AM), Laser Powder Bed Fusion (L-PBF), neutron diffraction, X-ray energy dispersive diffraction, stress redistribution.

1 Introduction

Additive manufacturing (AM) techniques have gained great importance in recent years for their unrivalled capability to produce complex-shaped components for automotive, medical, and

aerospace applications. AM processes allow the production of parts directly from a digital 3D model, minimizing both material wastage and the need for expensive subtractive tooling. Among the AM techniques, Laser Powder Bed Fusion (L-PBF) is a powder-based generative technique, in which the material is selectively melted by a laser beam (Q. Yan, 2020). L-PBF is widely used for the production of near-eutectic Al-Si alloy components, highly demanded due to attractive properties such as excellent corrosion resistance, processability and thermal conductivity (J. Fiocchi, 2021). Particular thermal cycles occur during the L-PBF process with extremely rapid heating and cooling (in the range of 10^3 – 10^7 K/s) and where simultaneous melting of the top powder layer and re-melting of previously solidified layers below is observed (T. DebRoy, 2018).

These characteristic processing conditions cause a very fine microstructure, consisting of α -aluminium small grains and, secondary, sub-grain cells preferentially solidifying along the $\langle 100 \rangle$ crystal direction towards the centre of the melt pool (P. Yang, 2018). The submicron aluminium cells are decorated by a nanometric silicon phase (with a diamond crystal structure) and enclosed by an almost continuous eutectic silicon network. Also, part of the Si and Mg atoms remains in a supersaturated solid solution in the aluminium matrix. The Si solubility was measured to be approximately 1–3 at.%, i.e. much higher than the equilibrium solubility (<0.1 at.% at room temperature), due to the fast cooling rates (L. Zhou, 2018). Therefore, in the as-built condition, an important fraction of the silicon is contained within the aluminium lattice. This fine distribution leads to high hardness, ultimate tensile strength and elongation at fracture, higher or at least comparable to the cast AlSi10Mg material (L. Thijs, 2013). Moreover, the L-PBF material exhibits an anisotropic mechanical behaviour: when the load is applied in the building direction, the elongation is comparable to that of the cast material, while when the specimen is loaded perpendicular to the building direction the elongation at fracture is almost 2% higher (K. Kempen, 2012).

When heating above 265 °C, the Si fraction in solid solution is progressively rejected from the matrix (Padovano 2020) (J. Fiocchi, 2021). After 1 hour, the process is almost completed, and the Si precipitated from the supersaturated matrix (F. Lasagni, 2008). Annealing at 265 °C preserves a relatively high tensile strength compared to the other heat treatments frequently performed before ageing, as for instance, a 1h 300 °C stress relief or 1h solutioning at about 500 °C. Some authors report that annealing at temperatures below 300 °C may be more advantageous for the removal of the RS while maintaining at the same time a relatively high strength thanks to the preservation of the silicon network (J. Fiocchi, 2021). Nevertheless, these

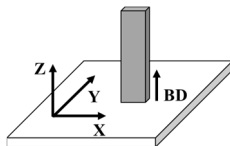
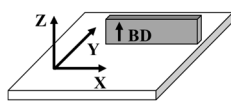
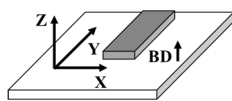
heat treatments do not take advantage of the age hardening provided by the precipitation of Mg_2Si when a full T6 heat treatment is applied (typically, 1h solutioning at about 500 °C followed by 8h ageing at ~180°C).

The complex and severe thermal cycles occurring during L-PBF processes lead to the build-up of significant residual stress (RS), which, if not controlled and accounted for, can prove highly deleterious to the fatigue strength of metal L-PBF components. A reinforcing combination between RS and the applied load can lead to unexpected failure. However, this also implies that the component life can be extended by removing harmful or even introducing beneficial RS (C. Li, 2018). For this reason, controlling the amount of RS is of extreme importance to the safe in-service operation of additively manufactured components. Moreover, proving the adequacy of L-PBF as-built microstructures (e.g., retaining the Si network) in terms of expected performance could be an attractive solution to reduce post-processing costs, or even envisage the development of new grades.

Extensive research has been dedicated in recent years to optimize the process parameters (such as scan strategy, preheating temperature and contour strategy) aiming to reduce the build-up of detrimental RS (N. Read, 2015) (S. Marola, 2021) (J. G. Santos Macias, 2020) (A. H. Maamoun, 2018) (M. Guo, 2019) (E. Beevers, 2018) (R. Casati, 2018). As an overall conclusion, a higher preheating temperature leads to lower RS magnitudes by reducing the severity of the thermal gradients occurring during the process. It has been reported that setting the build platform temperature to 200 °C yields a negligible RS level (J. G. Santos Macias, 2020) (A. H. Maamoun, 2018). For instance, *Zhao et al.* measured a strong reduction in the RS when the preheating temperature is increased: in samples manufactured with a building platform temperature at 35 °C the measured RS range is about 90 MPa, while higher preheating temperature at 200 °C reduces the RS to below 15 MPa. Moreover, for a fixed preheating temperature, a stripe scanning strategy produces higher RS compared to a chessboard strategy (M. Guo, 2019). *Beevers et al.* studied the influence of the so-called contour layer on the fatigue performance. Samples manufactured with contour contain larger near-surface defects than those found in samples produced without contour. Additionally, the roughness measured after polishing is higher if a contour is applied. Moreover, without contour, samples exhibit larger compressive RS at the surface in the load direction. The presence of smaller subsurface defects, the lower roughness, and the compressive RS, they all contribute to an improvement of the fatigue properties in specimens produced without contour (E. Beevers, 2018).

A summary of the as-built RS magnitudes reported in the open literature for L-PBF AlSi10Mg is given in **Fehler! Verweisquelle konnte nicht gefunden werden..** It is observed that the measured RS has a strong dependence on the part geometry, scan strategy, as well as build platform temperature.

Table 1. Summary of RS measurements on L-PBF AlSi10Mg reported in the literature.

Authors	T _{platform} (°C)	Scan strategy	Geometry	Building direction	Surface condition	Method	RS range: Maximum ÷ minimum (MPa)
(E. Beevers, 2018)	165	Stripes, rotation vector 67°	Hourglass	A	vibratory polishing, no contour	XRD	-140 ÷ -80 (Z direction)
					vibratory polishing, with contour		-50 ÷ -10 (Z direction)
(C. Li, 2018)	80	Chessboard, rotation vector 67°	Prism	C	As-built	XRD	20 ÷ 120 (X direction)
		Stripes, rotation vector 67°					40 ÷ 140 (X direction)
	120	Chessboard, rotation vector 67°					0 ÷ 90 (X direction)
	160	Chessboard, rotation vector 67°					-5 ÷ 50 (X direction)
(L. Zhao, 2020)	35	Stripes, rotation vector 67°	Prism	A	As-built	Compliance	-40 ÷ 50 (X direction)
	200					Compliance	-7 ÷ 5 (X direction)
(I. Roveda, 2022)	200	Chessboard, rotation vector 45°	Cylinder	A	As-built	XRD	-5 ÷ 25 (Z direction)
(C. Colombo , 2019)	150		Prism	B	As-built	XRD	70 ÷ 120 (Z direction)
				A			50 ÷ 110 (X direction)
<div><div><div>A</div><div>Building direction</div><div></div></div><div><div>B</div><div></div></div><div><div>C</div><div></div></div></div>							

Almost the entirety of the authors investigated the RS by laboratory X-ray diffraction. On an Al alloy, this technique allows one to probe to a depth of about 10 μm beneath the surface, i.e., surface RS are investigated. Alternatively, *Zhao et al.* performed RS analysis via the compliance method. In this case, a depth profile is measured on a plane at a selected height. Even though it is destructive to the part, this technique allows the analysis of bulk RS. It was observed that increasing the building platform temperature from 30 to 200 °C led to a reduction of 87% of the stress range, namely the difference between the maximum and the minimum value in the RS profile; this is reported to also happen in the bulk (see **Fehler! Verweisquelle konnte nicht gefunden werden.**).

Neutron diffraction has been proven to be a reliable tool to measure the long-range triaxial RS state within the bulk of metallic materials in a non-destructive manner (K. An, 2017) (F. Bayerlein, 2018). Obtaining a reliable measure of d_0 is, however, often not trivial, but the calculated RS are highly sensitive to this parameter. Common practices of determining d_0 include far-field measurements, where stress can be considered to be negligible, powders, a sample where the macrostress is relieved by mechanical slicing or calculations based upon force and moment balance (P. J. Withers, 2007). Herein, we decided upon two methods: (i) measuring coupons cut by electrical discharge machining (EDM) over the equivalent cross section (i.e., extracted from a sister specimen), and (ii) calculation of d_0 assuming a plane stress state at the free surfaces of the machined notch.

Moreover, also only few studies exist on the effect of low temperature (i.e., stress relief) post processing heat treatments on surface RS are published (C. Colombo, 2019) (I. Roveda, 2022). The results indicate that heat treatments above 245 °C led to a relaxation and redistribution of surface RS. However, the near-surface and bulk RS states of L-PBF AlSi10Mg material after post-processing heat treatment are not currently addressed in detail in the open literature. The study presented in what follows aims at filling this knowledge gap by providing a comprehensive analysis of the subsurface and bulk RS evolution after low-temperature heat treatment. Hence, the RS state in the as-built state is compared to that obtained after an annealing heat treatment at 265 °C for 1 hour. RS analyses are mainly performed by means of neutron diffraction, over selected cross section planes of single edge notch bending (SENB) fatigue crack growth specimens.

2 Material and methods

2.1 L-PBF AlSi10Mg samples production

The investigated samples were produced by a Concept Laser M2 machine at German Aerospace Research Center (Deutsches Zentrum für Luft- und Raumfahrt e.V., DLR), Germany. The samples were built on a platform using gas atomised AlSi10Mg powder under argon atmosphere. The scan strategy consisted of 5×5 mm² squares with 45° rotating scan vectors, as shown in Figure 1. The longest edge of the sample (height, 112 mm) is parallel to the building direction.

A laser power of 380 W with a scanning speed of 1500 mm/s was adopted. The layers had a 30 μ m thickness and the hatching distance is 100 μ m. The baseplate was kept at 200 °C during the entire process. The outer contours were scanned after the bulk with a standard contour strategy using a single scan with a laser power of 180 W and scanning velocity of 1600 mm/s.

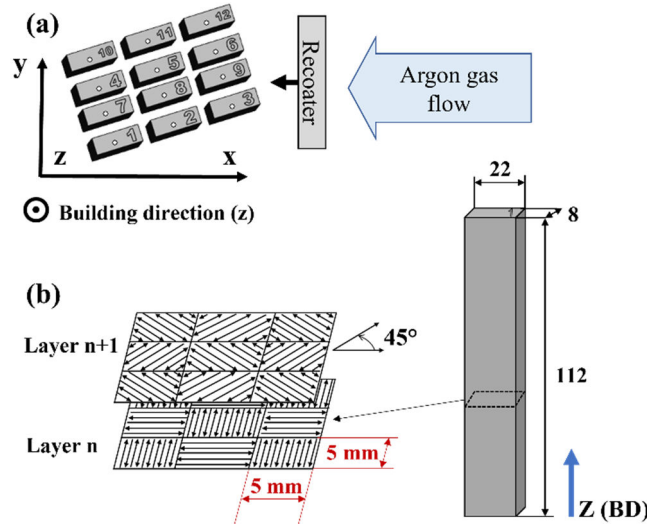


Figure 1. Sample production: (a) Positioning on the plate within the L-PBF chamber. (b) As-built AlSi10Mg prism geometry and scanning strategy.

Rectangular $22 \times 8 \times 112$ mm³ (width \times thickness \times height) prisms were printed and subsequently machined to a Single Edge Notch Bending (SENB) shape (Figure 1b) according to ISO12108 (ISO12108:2018, 2018). In addition to the as-built condition, a low-temperature annealing at 265 °C for 1 hour was performed, followed by air cooling with a cooling rate of 10 °C /min. In this case, the final SENB specimen was machined after the post-process heat treatment to avoid distortions.

2.2 Microstructural characterization

The effects of the heat treatment on the microstructure were investigated using a Scanning Electron Microscope (FEG-SEM) LEO 1530VP (Zeiss, Germany), operated under an acceleration voltage of 20 kV and a probe current of 7-8 μA in high pressure mode. The secondary electron (SE) imaging mode was used. Crystallographic information about the orientation and grain size was also acquired using Electron Backscattering Diffraction (EBSD). The EBSD data were acquired with an ESPRIT 1.94 (Bruker Nano) system using a Bruker e-FlashHR detector. Data analysis was performed using the Oxford Instruments HKL Channel 5 software (Oxford, 2008), as well as the MTEX Matlab toolkit (F. Bachmann, 2021).

The metallographic samples were extracted from the centre of a sister SENB sample. The preparation includes three initial polishing steps with silicon carbide abrasive grinding papers (1200, 2400 and 4000 grit), followed by a 3 μm diamond slurry on a polishing cloth, and a final step with a 0.2 μm colloidal silica suspension. To increase the contrast between the aluminium matrix and the silicon network, a final etching step was carried out using a Dix & Keller solution (190 ml H_2O ; 5 ml HNO_3 ; 10 ml HCl ; 2 ml HF) for 15 min.

The defect distribution was investigated through micro computed tomography (μCT). The tomograph was developed in-house at the Bundesanstalt für Materialforschung und -prüfung (BAM, Berlin, Germany); it features a Microfocus X-ray tube XWT-225-SE from X-Ray WorX GmbH (30827 Garbsen, Germany), with a focal spot of 6 μm and a maximum voltage of 225 kV, and a XRD1620 detector from PerkinElmer Inc. (Waltham, MA, USA) with a CsI scintillator of 2048 x 2048-pixel. The source-detector distance was fixed to 1170 mm. The voxel size obtained for a 6 mm thick SENB specimen was $(8 \mu\text{m})^3$. The software VGstudio MAX 3.0 from Volume Graphics, Heidelberg, D, (GmbH, 2019) was used to visualize and analyse the CT data.

2.3 Experimental set-up for Residual Stress analysis

The RS state was investigated at the subsurface and within the bulk of two SENB specimens, in as-built and heat-treated conditions. The Bulk RS were analysed by means of neutron diffraction (ND) using the Strain Analyser for Large Scale engineering Applications (SALSA) instrument at the Institute Laue-Langevin (ILL), France (I. Serrano-Munoz, 2021). Schematics of the set-up are shown in Figure 2a. The instrument uses a monochromatic beam and a Position Sensitive Detector (PSD) at a distance of 1 m from the sample. Using a neutron wavelength of approximately $\lambda = 1.66 \text{ \AA}$, the Al {311} diffraction peak (located at approximately $2\theta \approx 85.6^\circ$)

was utilized for strain measurement. The selection of Al {311} is based on the fact that this peak is least affected by intergranular strain (ISO-21432, 2019).

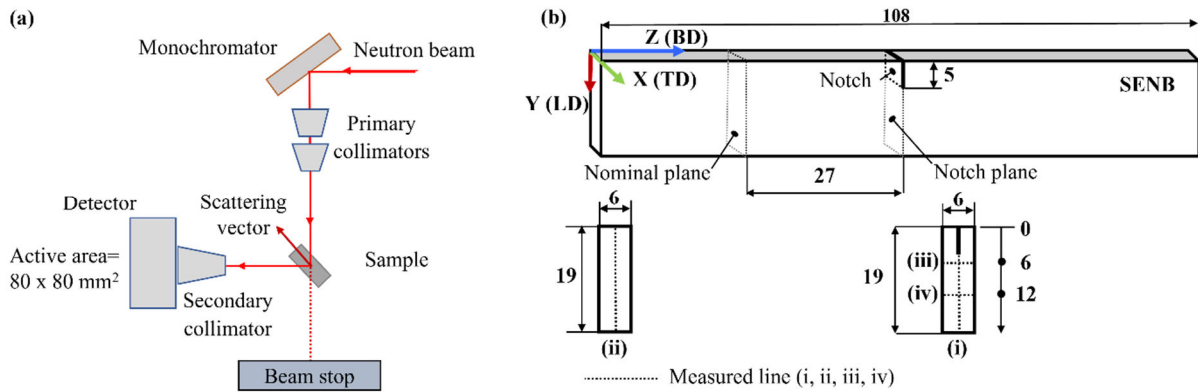


Figure 2: (a) Schematics of ILL-SALSA set-up. (b) Single Edge Notched Bending (SENB) specimen geometry and measured lines: along LD for (i) in the notch plane and (ii) in a nominal plane (i.e., 27 mm away from the notch); in the notch plane along TD at (iii) 1 mm ahead of the notch and (iv) 7 mm ahead of the notch.

Strains were measured in the three principal directions defined by the prism geometry: building direction (BD), transversal direction (TD) and longitudinal direction (LD). The four lines scanned are shown in Figure 2b: (i) a line at the notch plane, where the stress field is affected by the notch, and (ii) a line far from the influence of the notch, at a height of 27 mm (namely nominal plane). The variation through the 6 mm thickness (corresponding to TD) was also investigated at the notch plane on two lines: (iii) 1 mm ahead of the notch tip, to consider the influence of the notch, and (iv) 7 mm ahead the notch tip, where the stress field is assumed to be unaffected by the notch and the free surface.

Along lines (i) and (ii) strains were measured with pitches of 0.5 mm (near the notch) and 1 mm (remaining length). The counting time per point was 5 min. We used a gauge volume of $0.6 \times 2 \times 2 \text{ mm}^3$ for the measurements of BD and the TD. To maintain the same spatial resolution, the optics were rotated by 90° (to obtain a gauge volume of $2 \times 0.6 \times 0.6 \text{ mm}^3$) for the measurements along the longitudinal component (LD). The use of an elongated gauge volume in the BD was assumed appropriate as the residual stress is not expected to exhibit strong gradients along this direction over the measured length scale. A clarifying scheme of the optics arrangement is provided on the top of Figure 3.

The $2 \times 0.6 \times 0.6 \text{ mm}^3$ gauge volume and a pitch of 1 mm was used for the through-thickness measurements, lines (iii) and (iv) at the bottom of Figure 3. In this configuration the gauge volume diagonal in the TD direction was approximately 0.85 mm (Figure 3, bottom).

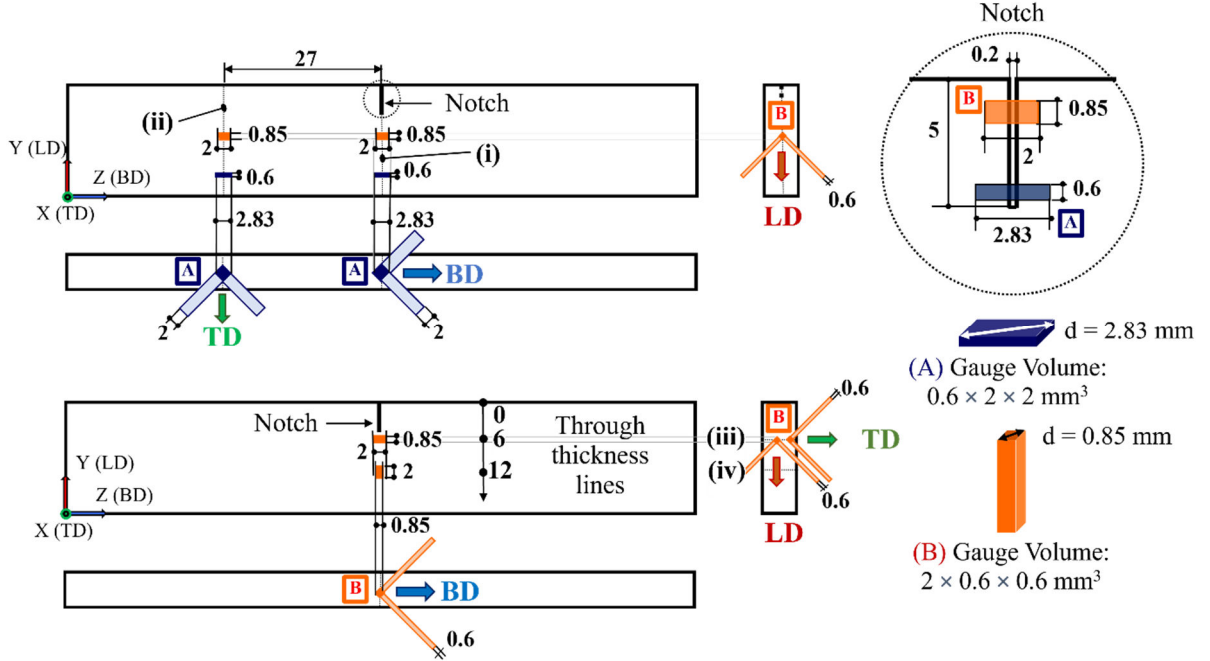


Figure 3: Schematics of the two configurations adopted for the ND measurements on SENB specimens. Two different gauge volumes were used: (A) $0.6 \times 2 \times 2 \text{ mm}^3$ and (B) $2 \times 0.6 \times 0.6 \text{ mm}^3$. For scan lines (i) and (ii) the gauge volume (B) was used for the BD and TD, afterwards the primary optic was rotated by 90° (gauge volume (A)) to measure TD (top of the image). Line (i) was measured also across the notch for the determination of the free-stress reference (the gauge volumes (A, B) included the notch and part of material as shown in the inset). For lines (iii) and (iv) the gauge volume (B) was used for all three directions (bottom of the image).

Importantly, line (i) was measured also across the notch for the determination of free-stress reference; in this case, the gauge volumes (A, B) included the notch and part of material (see inset in Figure 3).

By probing the specimen with a monochromatic neutron beam, lattice spacings (d_{hkl}) are determined from the measured angular position of the diffraction peak θ_{hkl} by applying the Bragg's law (first order peak):

$$(1) \quad \lambda = 2 \cdot d_{hkl} \cdot \sin \theta_{hkl}$$

A Gaussian function was fitted to the recorded diffraction peaks via using the in-house ILL software LAMP (Large Array Manipulation Program). The strain ε_{hkl} is calculated from the Bragg peak position as follows:

$$(2) \quad \varepsilon_{hkl} = \frac{d_{hkl} - d_{hkl,0}}{d_{hkl,0}} = \frac{\sin \theta_{hkl,0}}{\sin \theta_{hkl}} - 1$$

The RS components are then calculated according to the Hooke's Law as

$$(3) \quad \sigma_i = \frac{E}{1+\nu} \varepsilon_i - \frac{E \cdot \nu}{(1+\nu)(1-2\nu)} (\varepsilon_i + \varepsilon_j + \varepsilon_k)$$

The elastic constants were calculated using the Kröner model: $E = 69.390$ GPa and $\nu = 0.35$ for the Al {311} reflection (X.X. Zhang, 2021).

In addition to the bulk RS, the subsurface RS state was determined by energy-dispersive X-ray diffraction (EDXRD) at the X-ray Corelab, Helmholtz-Zentrum Berlin für Materialien und Energie (HZB), Berlin. The Corelab laboratory is equipped with a liquid-metal-jet X-ray source, which allows a penetration up to 500 μm in a lightweight aluminium alloy. Continuous polychromatic X-ray radiation of up to 160 keV is generated by Bremsstrahlung. In the reflection geometry, residual stress depth profiles in the near-surface region up to some hundred micrometres can be obtained. The results shown in this study relate to the Al {311} peak, associated to a penetration depth of about 350 μm . The measurements were performed with a 1 mm pinhole polycapillary and a constant diffraction angle of $2\theta = 16.6^\circ$. The measurement time per point was 5 min. For the energy dispersive case, Bragg's law can be rewritten using $E = h\nu = hc/\lambda$. By substituting such relation in Equations

(1) and (2), the lattice spacing can be obtained from the energy as follows:

$$(4) \quad d_{hkl} = \frac{6.199}{\sin \theta} \cdot \frac{1}{E_{hkl}}$$

The $\sin^2\psi$ method is then utilized for RS determination, assuming a biaxial stress condition as RS are measured at the near surface (the stress component normal to the free surface is assumed to be negligible). The subsurface RS were measured on a line ahead of the notch tip with a pitch of 5 mm.

2.4 Stress-free reference (d_0) determination

When the bulk RS of the material is probed, a stress-free reference must be used for the strain calculation (see Equation (2)). Two different strategies were adopted for the ND stress-free reference (d_0) determination.

Firstly, a 2 mm thick slice was extracted from the central part of a sister as-built SENB sample (see Figure 4). Using electrical discharge machining, EDM, small $2 \times 2 \times 2 \text{ mm}^3$ interconnected coupons were cut according to the pattern shown in Figure 4. This strategy ensures relief of macro-stresses and is strongly advised for neutron diffraction measurements since it allows detecting local variations of d_0 arising from compositional or microstructural gradients. A $2 \times 0.6 \times 0.6 \text{ mm}^3$ gauge volume was used to analyse the coupons, as shown at the bottom of Figure 4.

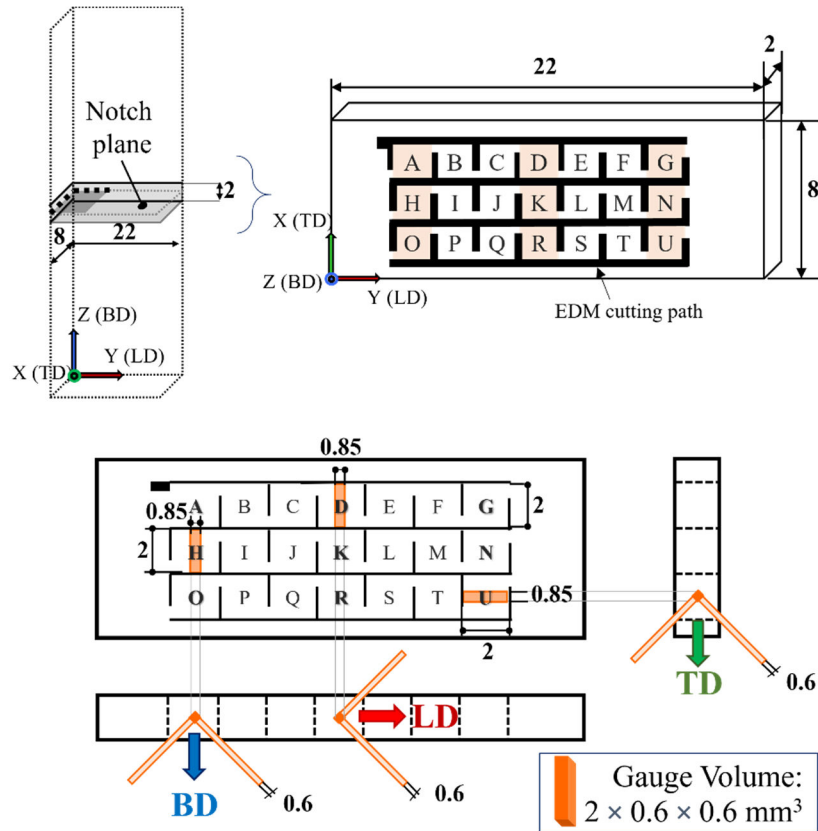


Figure 4: Grid of interconnected coupons for the determination of the stress-free reference d_0 : location of the extracted material in the sister specimen (top left), specimen geometry (in mm, top right), and measurement strategy (bottom).

Secondly, d_0 can be calculated by exploiting the plane-stress boundary condition which can be assumed at the notch faces. At the two free surfaces inside the notch, the component perpendicular to the surface, namely BD, is assumed to be negligible. Therefore, σ_{BD} can be

approximated to zero at this location. The three strain components in the principal geometrical directions were measured using the same gauge volumes as described for line (i) (Figure 3, top).

Considering the equations in 2.3 and replacing the strain components in Equation (3) with the expression in Equation (2), the following equation can be written:

$$(5) \quad \sigma_i = \frac{E}{1+\nu} \left[\frac{d_i}{d_0} - 1 + \frac{\nu}{(1-2\nu)} \left(\frac{d_i}{d_0} - 1 + \frac{d_j}{d_0} - 1 + \frac{d_k}{d_0} - 1 \right) \right]$$

If $\sigma_{BD} = 0$, d_0 can be calculated from the lattice spacing measured within the notch in the three directions: d_{BD} , d_{TD} , d_{LD} (G. Albertini, 1997) (K. An, 2017):

$$(6) \quad \sigma_{BD} = \frac{E}{1+\nu} \left[\frac{d_{BD}}{d_0} - 1 + \frac{\nu}{(1-2\nu)} \left(\frac{d_{BD}}{d_0} - 1 + \frac{d_{TD}}{d_0} - 1 + \frac{d_{LD}}{d_0} - 1 \right) \right] = 0$$

$$(7) \quad d_0 = \frac{1-2\nu}{1+\nu} \left[d_{BD} + \frac{\nu}{1-2\nu} (d_{BD} + d_{TD} + d_{LD}) \right]$$

The second strategy was applied to both the as-built and the heat-treated specimens.

3 Results and discussion

3.1 Microstructure

SEM micrographs were taken in the as-built and heat-treated conditions from the fine melt pool zone, both in the cross-section (direction.

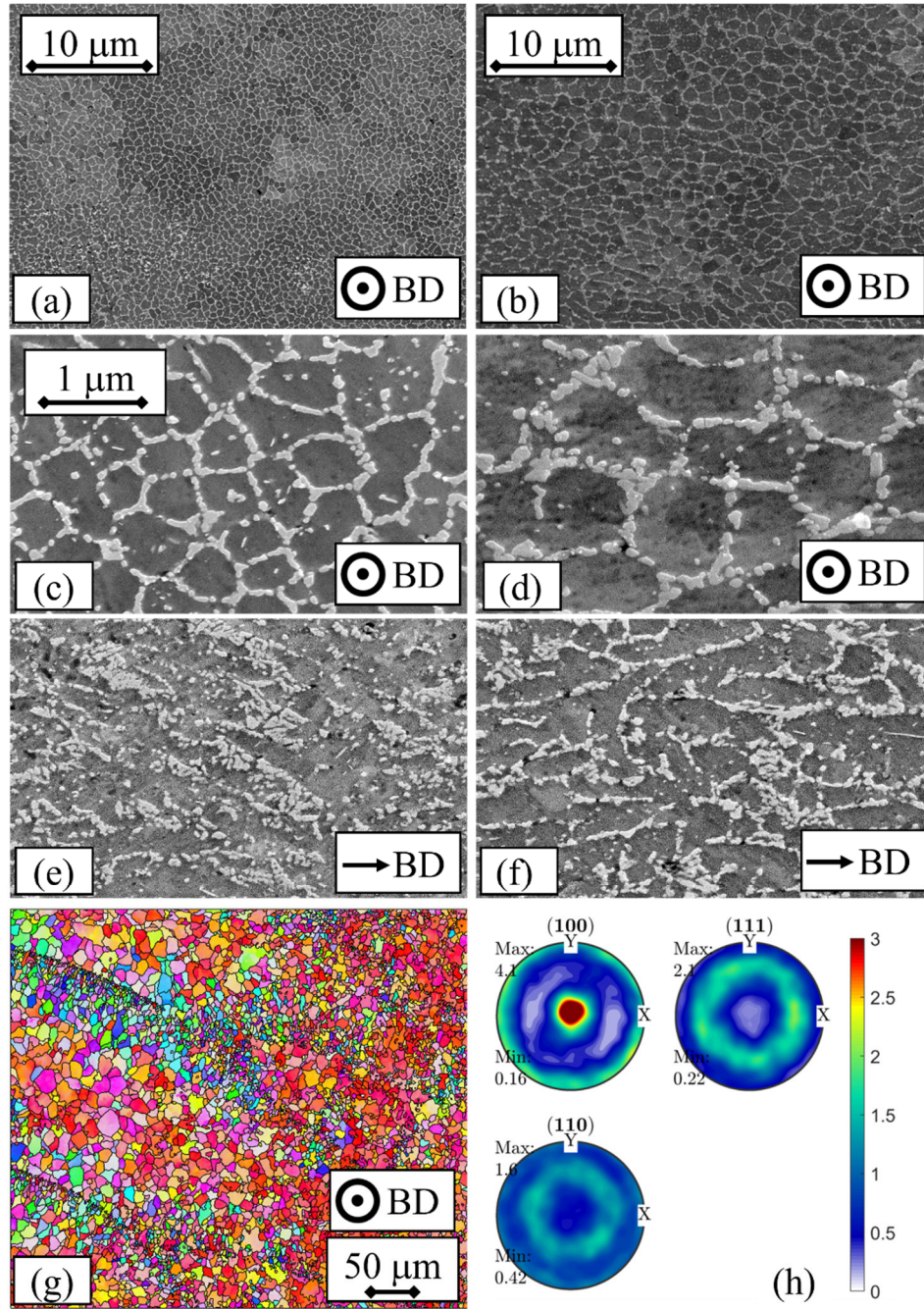


Figure 5a,b,c,d) and along the building direction (Figure 5e,f). In the as-built state (Figure 5a,c,e) the aluminium matrix (in dark grey) is supersaturated with Si and Mg atoms. The aluminium cells contain very fine entrapped eutectic Si particles with a diameter generally smaller than 20 nm. A nano-sized intercellular eutectic Si network, mostly interconnected, envelops the matrix cells. After 1 hour annealing at 265 °C, the interconnected microstructure underwent some minor changes (Figure 5b,d,f) (L. Zhao J. G., 2019). The Si fraction in solid solution precipitates from the matrix as investigated in literature by Differential Scanning Calorimetry analyses (R. Casati, 2018) (M. Pellizzari, 2020) (S. Marola, 2021) (J. Fiocchi, 2021). The EBSD orientation map in Figure 5g shows that the grain size gradually coarsens

from the melt pool boundary towards the middle of the melt pool. The pole figures in Figure 5h show a moderately strong $\langle 100 \rangle$ fibre texture along the building direction. Such texture is predominant near the melt-pool centre, where the cells growth direction is more closely aligned with the overall heat flow direction (H. Qin, 2018).

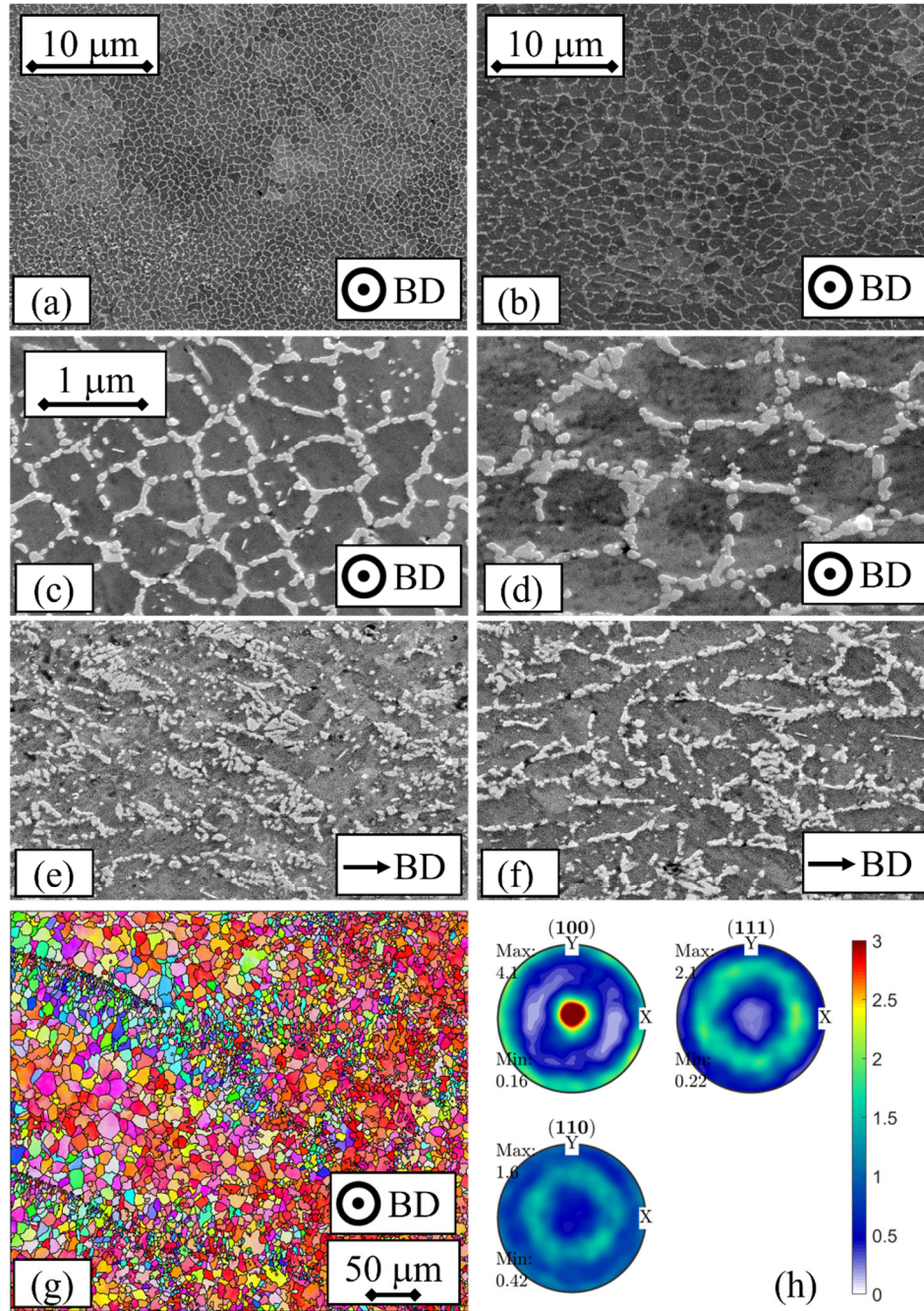


Figure 5: AlSi10Mg SEM-SE micrographs in the as-built condition (a,c) in the cross-section at different magnifications and (e) along the building direction; and after heat treatment at 265 °C for 1 hour in the (b,d) cross-section at different magnifications and (f) building direction. (g) orientation map on the cross section in the as-built condition, with (h) the respective (100), (110) and (111) pole figures.

The void distribution in a sister SENB specimen is shown in Figure 6. The μ CT evaluation focussed on the defects in the region probed by the neutron beam during RS measurements. In the measurement along the LD the gauge volume covers an area of $\sim 2 \times 2 \text{ mm}^2$ in the BD-TD plane. Considering this fact, the defects content in a similar region is projected on a 2D plane using the *thick slab* option contained in VGSTUDIO. The ND probed region is shown in orange in Figure 6 and the gauge volume projection is represented with a red rectangle. In this way, defects clusters are revealed (porosity is shown in black). The detected defects are almost entirely spherical pores (the average diameter is $50 \text{ }\mu\text{m}$ and the porosity volume fraction is 0.15%) mostly located at the boundaries between adjacent islands of the chessboard scanning pattern. These pores can be associated to excessive volumetric energy densities during the process (K. V. Yang, 2018). The projection of pores in the BD (top view in Figure 6b) and TD (front view in Figure 6c) highlights this preferential zone of pore formation. When considering the volume probed by the beam during neutron diffraction, the defects are aligned in $\sim 0.5 \text{ mm}$ wide lines recurring approximately every 1 mm .

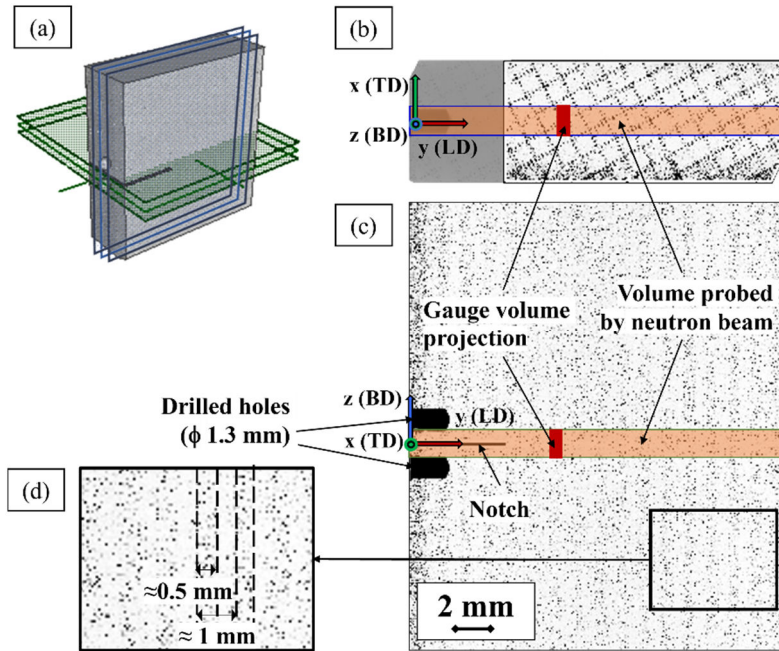


Figure 6: (a) 3D rendering and orthographic projections in the BD (b) and TD (c) of a μ CT reconstruction of a sister SENB specimen. In the front view (c) all the defects in the vertical plane contained within a $\pm 1 \text{ mm}$ depth from the central plane (blue planes in (a)) are projected along TD. In the top view (b) the defect content in a region of a depth $\pm 1 \text{ mm}$ from the notch plane are projected along BD (area enclosed between the green planes in (a)).

3.2 Stress-free reference d_0

The d_0 stress-free reference for the as-built condition was measured using nine of the coupons of the grid described in Section 2.3, namely A-D-G-H-K-N-O-R-U (Figure 4). Note that the LD component was measured only in three coupons (H-K-N). The spatial variation of d_0 -spacing along BD, TD and LD is shown in Figure 7. A slight anisotropy between the BD and the other two components is observed: the average d_0 in the BD is equal to 1.21386 ± 0.00006 Å, higher than the measured value in the TD and LD (1.21337 ± 0.00006 Å and 1.21339 ± 0.00006 Å, respectively, and therefore equal). As seen in Section 3.1, the grains are elongated in the BD, growing preferentially in the $\langle 100 \rangle$ direction. This morphological and crystallographic anisotropy in the BD is reflected in the RS fields: the BD component is higher compared to LD and TD. A dependence of the lattice spacing on the measurement direction has been also found in other AM materials such as IN718 and 316L (T. Thiede, 2018) (A. Ulbricht, 2020) (F. Bayerlein, 2018) (L. M. Sochalski-Kolbus, 2015). As the difference between the components is small (lower than 0.05%), d_0 is calculated as the arithmetic average of the three orthogonal directions (Z. Wang., 2017) (T. Thiede, 2018) (A. K. Syed, 2019) (A. Ulbricht, 2020). The d_0 -spacing obtained averaging all the measurements in all three main directions is $d_0 = 1.2135 \pm 0.0005$ Å.

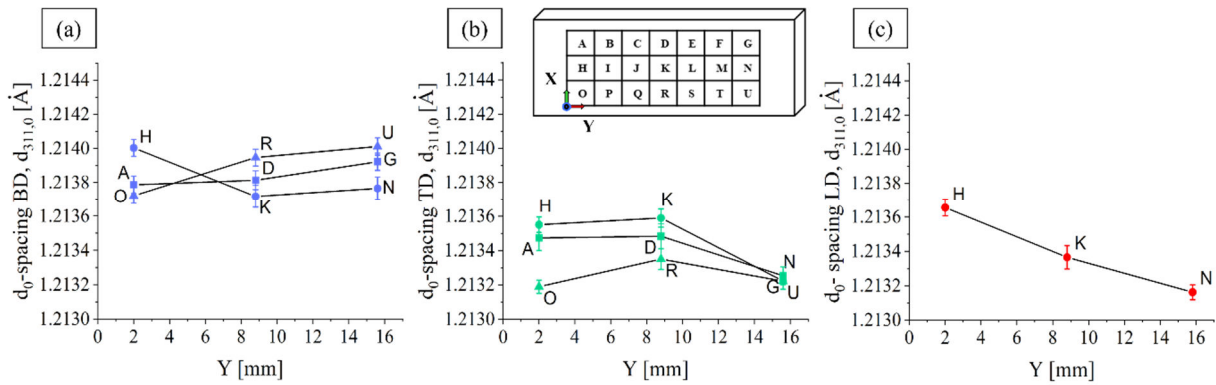


Figure 7: As built condition: d_0 -spacing against the position of coupons along the Y-axis, for the (a) BD, (b) TD, and (c) LD.

The d_0 variability on the cross-section corresponds to a maximum stress variation of about ± 20 MPa.

The contour plot of Figure 8a shows the d_0 variability on the cross-section for the TD component in the as-built condition. This plot is compared with the distribution of pores (see Figure 8b,c). Interestingly, the density of defects is higher close to the contour layer, on the top part of the grid (coupons A-D-G) and, more pronouncedly, at the bottom (coupons O-R-U), where the d_0 -spacing is also smaller compared to the central line (H-K-N). Thus, an increased

content of porosity, in addition to a composition spatial variation, are suspected to jointly affect the d_0 values. However, effects of porosity cannot be decoupled from the chemical variations in the cross-section. Complex processes such as AM can lead to local variations of the chemical composition within the same component (e.g., light elements like Mg that are susceptible to evaporation (Z. Wang, 2017) (N. T. Aboulkhair, 2014)). Material solidification is inhomogeneous, since the cooling rates are dependent on the position toward the center of the melt pool, the distance from the building platform and from the edges of the part (P. Mercelis, 2006), as well as the direction in which the inert gas flows during the building process (A. Ladewig, 2016). In the case of Al-Si alloys, the supersaturation of Si in the matrix depends on the cooling rates: faster cooling rates retain a higher proportion of alloying elements in a solid solution state (L. Zhou, 2018). A difference in the content of solid solution Si atoms in the Al matrix can modify the lattice spacing leading to local differences of d_{hkl} . Re-melting and re-heating of previously solidified layers leads to a further redistribution of the silicon content.

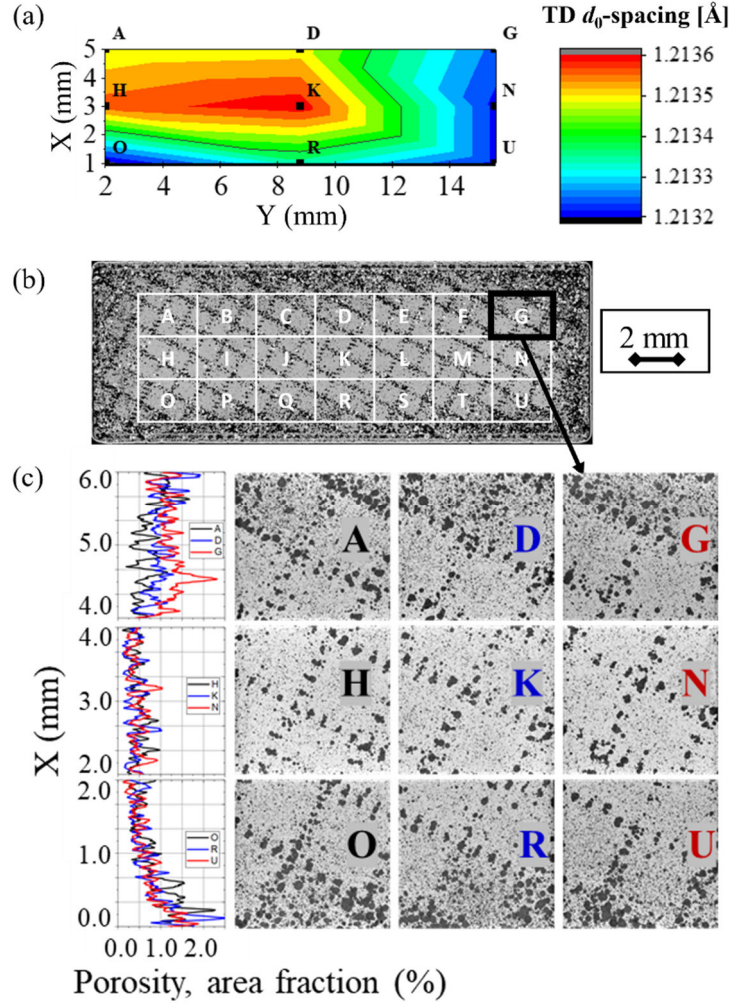


Figure 8: (a) Contour plot of the d_0 -spacing in the TD for the as-built condition. The average error of d_0 spacing is $\pm 0.00006 \text{ \AA}$. (b) Porosity spatial distribution as obtained by a projection of the pores contained in a 2 mm thick slice of a μ CT reconstruction. (c) Enlargement of (b) for the nine measured coupons with the respective porosity area fraction (left, in graph).

Moreover, typically, type I stresses (long range macrostresses) can be relieved by mechanical sectioning. However, type II (grain-scale intergranular) and type III (sub-grain scale) stresses are retained even when after cutting (P. J. Withers, 2007). In the case of a multi-phase material, an inhomogeneous strain partitioning between the phases due to the constraining effect of the stiffer Si phase on the more compliant Al matrix leads to interphase stresses. Therefore, in addition to possible chemical variations and porosity effects, these micro-residual stresses (type II) can also contribute to the observed scatter (Figure 8).

The second strategy to obtain d_0 was to apply boundary conditions at the notch: a line containing the notch (5 points measured along the line) was measured and the weighted average (Equation(7)) of the three components was considered as stress-free reference. The resulting d_0

is equal to $1.2132 \pm 0.0002 \text{ \AA}$ for the as-built condition and to $1.2134 \pm 0.0007 \text{ \AA}$ for the heat-treated condition.

The values of d_0 obtained with the two strategies (coupons and boundary condition), for the as-built condition, are compared in Table 2. The relative error between the two estimated values is considered negligible, as it is lower than 0.03%. Interestingly, the HT does not seem to alter d_0 .

Table 2: Results of the stress-free reference d_0 measured with different strategies.

Condition	d_0 strategy	d_0 -spacing (\AA)			Mean d_0 -spacing value (\AA)
		BD	TD	LD	
As-built	Coupons	$1.21386 \pm$	$1.21337 \pm$	$1.21339 \pm$	1.2135 ± 0.0005
		0.00006	0.00006	0.00006	
	Notch	$1.21327 \pm$	$1.21309 \pm$	$1.21330 \pm$	1.2132 ± 0.0002
		0.00006	0.00006	0.00006	
Heat-treated	Notch	$1.21346 \pm$	$1.21285 \pm$	$1.21365 \pm$	1.2134 ± 0.0007
		0.00006	0.00006	0.00006	

In order to arbitrate on the most reliable d_0 value, other boundary conditions can be exploited. Since at the specimen surfaces the plane stress condition must be met, the LD component should tend to zero as it approaches the free lateral surface. Furthermore, given the thin-walled geometry of the SENB specimens (6 mm thickness), the stress state should approach an overall plane stress condition (G. Albertini, 1997), where the TD stress should be negligible (R.J. Moat, 2011). These boundary conditions are broadly fulfilled when the d_0 resulting from the notch boundary condition is used, and this is why this d_0 is used as reference for the notch filed in what follows.

3.3 Near-surface RS by Energy-dispersive laboratory X-ray

The subsurface RS determined in the as-built condition by the $\sin^2\psi$ method using energy dispersive XRD are reported in Figure 9. The RS were measured in the BD and LD, along a line ahead of the notch, on the front and back surfaces of the specimen. The near-surface region exhibits the lowest compressive RS at point 1 (the nearest to the notch), whereas RS stabilises at -50 MPa in the LD component and at -35 MPa in the BD at the other three measured points. Comparable values were found on the opposite surface, thus only the RS profile on one side is shown in **Fehler! Verweisquelle konnte nicht gefunden werden.**

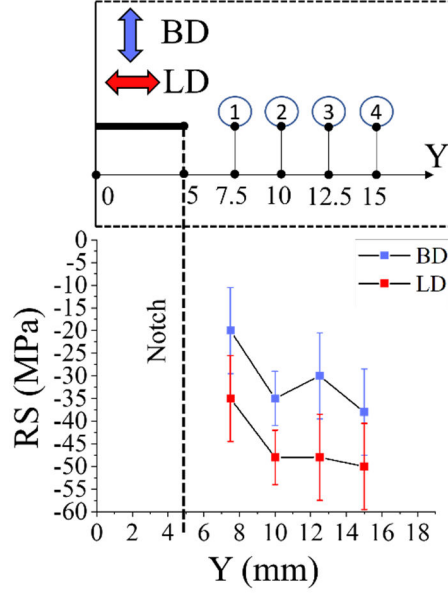


Figure 9: Near-surface RS along a line ahead of the notch in the SENB specimen, for the as-built condition.

3.4 Bulk RS by Neutron Diffraction

The profiles of all stress components along lines (i) - nominal field - and (ii) - within the notch plane (see Figure 2) - for both the as-built and heat-treated condition are given in Figure 10. Regardless of some marked fluctuations (e.g., BD component at $Y = 15$ mm), the RS in the as-built condition tends to be tensile, exhibiting magnitudes close to 20 MPa in the notch field and close to 10 MPa in the nominal field. The heat treatment mainly results in sign reversal of the stress: tensile stresses become compressive with an average magnitude of -10 MPa. Nevertheless, the influence of the notch is more pronounced in the heat-treated condition since the stresses are tensile in the close vicinity of the notch but become compressive at greater lengths. In contrast, for the AB condition, the stresses remain tensile across the whole notch field.

It must be noted that adopting the d_0 resulting from the notch boundary condition, the nominal field in the as-built condition would shift about 20 MPa towards higher tensile values, thereby not fulfilling stress balance within the section. Thus, the nominal profile needed to be corrected by applying additional boundary conditions, as discussed in Section 3.2. In this case, the discrepancy could be caused by a chemical variation through the height (BD) of the sample leading to different d_0 at the nominal and notch planes (N. T. Aboulkhair, 2014) (Z. Wang., 2017) (F. Bosio, 2021).

It is also observed that the calculated as-built ND RS are low (maximum values of 60 MPa), in agreement with the results shown in the literature for specimens produced using chess-board scanning strategy, contour layer and high temperature (200 °C) of the building platform (J. G. Santos Macias, 2020) (A. H. Maamoun, 2018) (M. Guo, 2019).

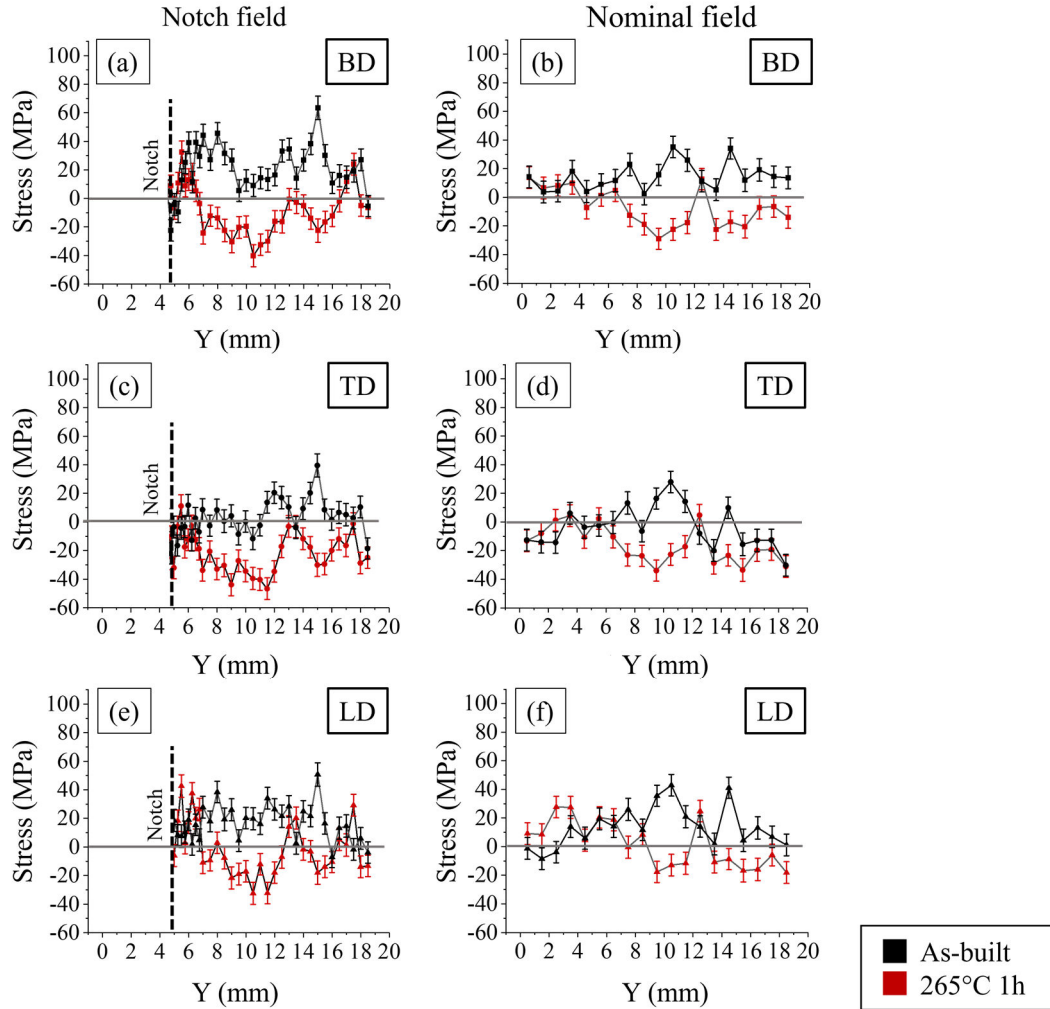


Figure 10: RS profiles: (a) BD for the notch plane, (b) BD for the nominal plane, (c) TD for the notch plane (d) TD for the nominal plane, (e) LD for the notch plane and (f) LD for the nominal plane. The two conditions are given: as-built (in black) and heat-treated (in red).

Although differences in the profiles of all stress components before and after heat treatment can be observed, the stress *ranges* (difference between maximum and minimum value in a profile) and the von Mises (vM) stresses (Figure 11) are not significantly affected by the heat treatment: a redistribution rather than a relaxation of stresses seems to occur. In the case of the notch plane, von Mises stresses vary between 10 and 40 MPa. The points located close to the notch (5 to 10 mm) generally exhibit stresses on average of 25 MPa, decreasing to 15 MPa in the region from 10 to 19 mm. While this difference lays within the error bar, it seems reasonable that the vM

stress increases near the notch tip. The negligible difference in vM stress between the as-built and heat-treated condition can be explained by the fact that a symmetrical redistribution occurs in the three main stress directions after heat treatment; i.e., the variation at each point is of the same magnitude for all three components. Thus, it can be considered that the changes observed mostly result from a modification of the interphase stresses: a repartition of the stresses between silicon and aluminium can be hypothesized. The precipitation of the Si from the aluminium matrix could induce a change in the stress repartition between the two phases (Figure 10).

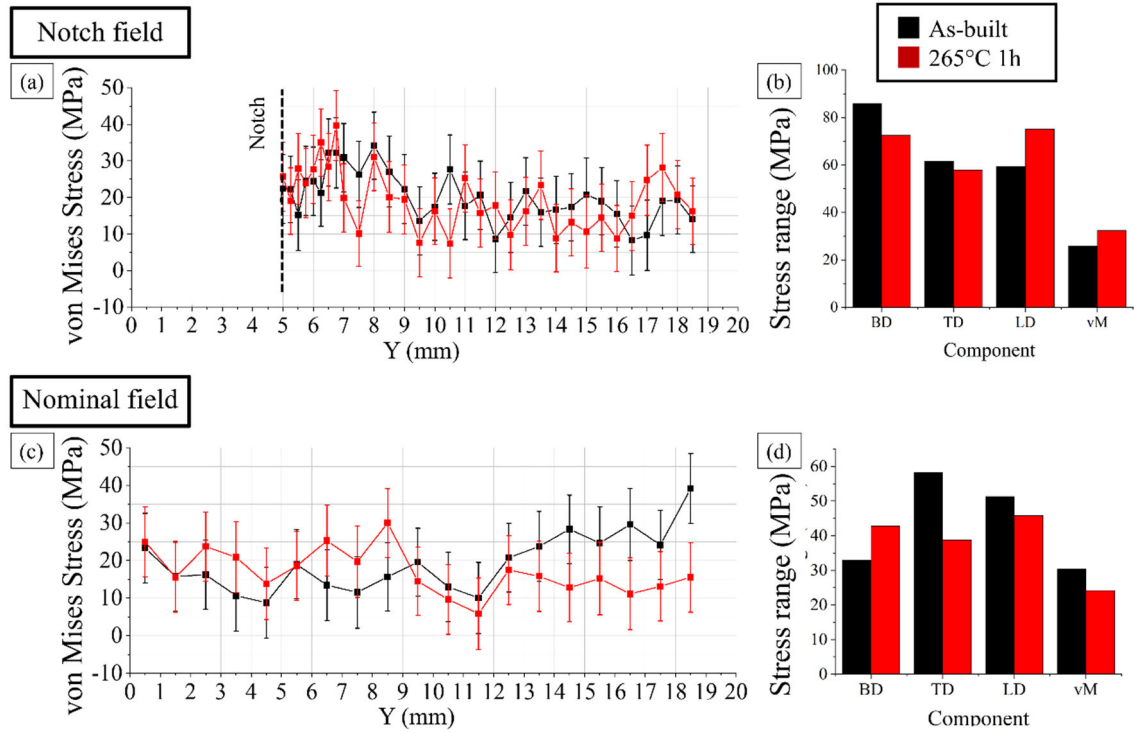


Figure 11: von Mises stress profiles along LD for the notch plane (a) and the nominal plane (c) for the as-built (black) and heat-treated (red) SENB. Stress ranges for the BD, TD and LD components: difference between the maximum and the minimum value measured in the notch plane (b) and in the nominal plane (d).

Additionally, the scatter found in the as-built condition is retained after heat treatment. In this regard, these oscillations have a periodicity that it is considered not compatible with the nanoscale (e.g., compositional variation affecting d_0 spacing typically occur as a spatial gradient rather than as a scatter), the microscale (e.g., silicon network arm spacing ≈ 100 nm and aluminium cells ≈ 1 μ m) or mesoscale (e.g., melting pool width ≈ 100 μ m) features. Considering the tomograms shown in Figure 6, the fluctuations in the measurements are most likely related to the macroscale. In this case, the defects align preferentially along lines with a width of ~ 0.5 mm, recurring approximately every 1 mm. Consequently, in some of the measured points, the volume probed by the beam during neutron diffraction may be immersed in an area with higher concentration of defects, leading to a punctual fluctuation of the measured strain value. The effect of such variation is explained further in

Figure 12: the BD stress component closely follows the periodicity of the porosity distribution.

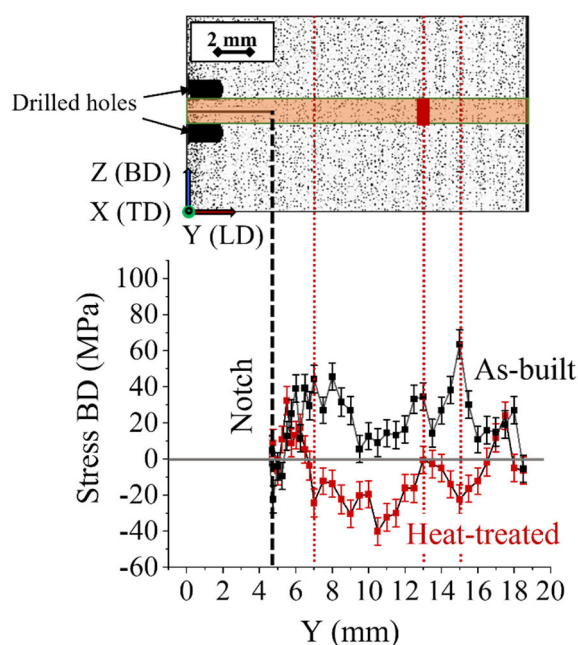


Figure 12: Comparison between the projection of pores in the TD and the RS profile in the BD.

Finally, the through-thickness profiles of the vM stress and the through-thickness stress ranges of all stress components are shown in Figure 13. In the as-built condition, the profiles exhibit an asymmetry from the left (e.g. in line (iii) in Figure 2 the 0.5 mm point at about 40 MPa) to the right (5.5 mm point at about 5 MPa) that is most probably related to the porosity-induced scatter described above. In the heat-treated conditions the profiles are flatter, especially away from the notch, where the vM are constant along the TD and equal to 15 MPa. Also in this case, we observe that the heat-treatment does not have a considerable impact on the values of the stress ranges (Figure 13b).

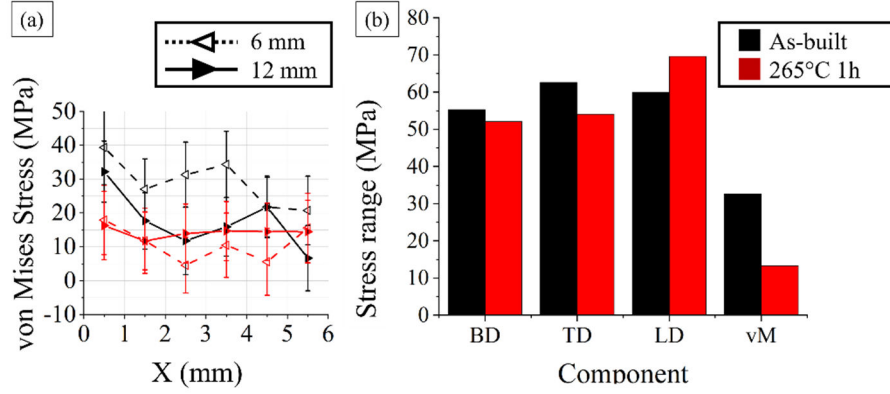


Figure 13: (a) von Mises stress profiles along X-axis of the as-built (black) and heat-treated (red) SENB at two different scan lines (see Figure 2) and (b) Through-thickness stress ranges for the BD, TD, LD and vM.

4 Conclusions

In this study a comprehensive analysis of the RS state using fatigue crack propagation AlSi10Mg specimens was presented. The near-surface and the bulk stress were investigated by energy-dispersive X-ray and neutron diffraction, respectively. The effect of an annealing heat treatment at 265 °C for 1 h to the bulk RS state was studied.

The absolute RS in the as-built condition tends to be in tension in the bulk (15 MPa in average) and compressive at the surface (-40 MPa in average), whereas, after heat treatment, the absolute stress components in the bulk evolve into compression. Although a shift in the absolute RS profiles is observed, the as-built and the heat-treated specimens show similar results when comparing them in terms of von Mises stresses and stress ranges. This implies that the distortion energy is not reduced by annealing. We hypothesize that a repartition of the stresses occurs between the two main phases, whose morphology is affected by the heat treatment.

In addition, the bulk stresses exhibit considerable scatter. It is proposed that the fluctuations could be caused by the porosity content: variations in the defect distribution within the volume probed by the neutron beam influences the average of lattice spacing at each measurement point. Future work intends to examine the resulting fatigue crack propagation performance of the two conditions as a function of RS state and microstructure.

Acknowledgements

This work is supported by internal Bundesanstalt für Materialforschung und –prüfung (BAM) funding (MIT1-2019-40). The Institute Laue-Langevin (ILL), France is acknowledged for Neutron diffraction beamtime on SALSA (I. Serrano-Munoz, 2021). The Helmholtz-Zentrum Berlin für Materialien und Energie is acknowledged for granting access to the LIMAX-160 instrument at the X-Ray Corelab Facility. Romeo Saliwan Neumann (Bundesanstalt für Materialforschung und -prüfung, Berlin (BAM), Germany) is acknowledged for his advice and technical assistance during the SEM microstructural investigation. Björn Mieller (Bundesanstalt für Materialforschung und -prüfung, Berlin (BAM), Germany) is acknowledged for performing the heat treatments.

References

- A. H. Maamoun, M. E. (2018). Thermal Post-processing of AlSi10Mg parts produced by Selective Laser. *Additive Manufacturing*, 21, 234–247.
- A. K. Syed, B. A. (2019). An experimental study of residual stress and direction-dependence of fatigue crack growth behaviour in as-built and stress-relieved selective-laser-melted Ti6Al4V. *Materials Science and Engineering: A*, 755, 246-257.
- A. Ladewig, G. S. (2016). Influence of the shielding gas flow on the removal of process by-products in the selective laser melting process. *Additive Manufacturing*, 10, 1-9.
- A. Ulbricht, S. J.-M. (2020). Separation of the Formation Mechanisms of Residual Stresses in LPBF 316L. *Metals*, 10, 1234.
- C. Colombo, C. A. (2019). Effect of Optimized Heat Treatments on the Tensile Behavior and Residual Stresses of Selective Laser Melted AlSi10Mg Samples. *Key Engineering Materials*, 813, 364-369.
- C. Li, Z. L. (2018). Residual Stress in Metal Additive Manufacturing. *Procedia CIRP*, 71, 348-353.
- E. Beevers, A. D. (2018). Fatigue properties and material characteristics of additively manufactured AlSi10Mg – Effect of the contour parameter on the microstructure, density, residual stress, roughness and mechanical properties. *International Journal of Fatigue*, 117, 148-162.
- F. Bachmann, R. H. (2021). Texture Analysis with MTEX - Free and Open Source Software Toolbox. *Solid State Phenomena*, 160, 63-68.
- F. Bayerlein, F. B. (2018). Transient Development of Residual Stresses in Laser Beam Melting - A Neutron Diffraction Study. *Additive Manufacturing*, 24, 587-594.

- F. Bosio, H. S. (2021). Production Strategy for Manufacturing Large-Scale AlSi10Mg Components by Laser Powder Bed Fusion. *JOM*, 73, 770–780.
- G. Albertini, G. B. (1997). Comparative neutron and X-ray Residual stress measurements in AA-2219 welded plate. *Materials Science Engineering A*, 224, 157-165.
- G. Requena, G. G. (2009). 3D Architecture and Load Partition in Eutectic Al-Si Alloys. *Advanced Engineering Materials*, 11, 1007-1014.
- GmbH, V. G. (2019). *VGSTUDIO MAX*. Retrieved from <https://www.volumegraphics.com/en/products/vgsm.html>
- H. Qin, V. F. (2018). Solidification pattern, microstructure and texture development in Laser Powder Bed Fusion (LPBF) of Al10SiMg alloy. *Materials Characterization*, 145, 29-38.
- I. Roveda, I. S.-M. (2022). Investigation of residual stresses and microstructure effects on the fatigue behaviour of a L-PBF AlSi10Mg alloy. *Procedia Structural Integrity*, 38C, 564-571.
- I. Serrano-Munoz, S. C. (2021). Effect of as-built residual stress state on the fatigue response of a LPBF AlSi10Mg alloy. *Institut Laue-Langevin (ILL)*. doi:10.5291/ILL-DATA.1-02-338
- ISO12108:2018. (2018). Metallic materials — Fatigue testing — Fatigue crack growth method. 77.040.10 *Mechanical testing of metals*, 53.
- ISO-21432. (2019). Non-Destructive Testing—Standard Test Method for Determining Residual Stresses by Neutron Diffraction; International.
- J. Fiocchi, A. T. (2021). Heat treatment of aluminium alloys produced by laser powder bed fusion: a review. *Materials and Design*, 204, 109651.
- J. G. Santos Macias, T. D. (2020). Influence on microstructure, strength and ductility of build platform temperature during laser powder bed fusion of AlSi10Mg. *Acta Materialia*, 201, 231-243.
- K. An, L. Y. (2017). Neutron residual stress measurement and numerical modeling in a curved thin-walled structure by laser powder bed fusion additive manufacturing. *Materials and Design*, 135, 122-132.
- K. Kempen, L. J.-P. (2012). Mechanical properties of AlSi10Mg produced by Selective Laser Melting. *Physics Procedia*, 39, 439 – 446.
- K. V. Yang, P. R. (2018). Porosity formation mechanisms and fatigue response in Al-Si-Mg alloys made by selective laser melting. *Materials Science and Engineering: A*, 712, 166-174.
- L. M. Sochalski-Kolbus, E. A. (2015). Comparison of Residual Stresses in Inconel 718 Simple Parts Made by Electron Beam Melting and Direct Laser Metal Sintering. *Metallurgical and Materials Transactions A volume*, 46, 1419-1432.

- L. Thijs, K. K. (2013). Fine-structured aluminium products with controllable texture by selective laser melting of pre-alloyed AlSi10Mg powder. *Acta Materialia*, 61, 1809–1819.
- L. Zhao, J. G.-L. (2020). Comparison of residual stresses obtained by the crack compliance method for parts produced by different metal additive manufacturing techniques and after friction stir processing. *Additive Manufacturing*, 36, 101499.
- L. Zhou, A. M. (2018). Microstructure, precipitates and hardness of selectively laser melted AlSi10Mg alloy before and after heat treatment. *Materials Characterization*, 143, 5-17.
- M. Guo, X. J. (2019). Microstructure, Mechanical Properties and Residual Stress of Selective Laser Melted AlSi10Mg. *Journal of Materials Engineering and Performance*, 28, 6753-6760.
- N. Read, W. W. (2015). Selective laser melting of AlSi10Mg alloy: Process optimisation and mechanical properties development. *Materials & Design*, 65, 417-424.
- N. T. Aboulkhair, N. M. (2014). Reducing porosity in AlSi10Mg parts processed by selective laser melting. *Additive Manufacturing*, 1-4, 77-86.
- O. I. (2008). HKL Channel 5. *SP9E*.
- P. J. Withers, M. P. (2007). Methods for obtaining the strain-free lattice parameter when using diffraction to determine residual stress. *Journal of Applied Crystallography*, 40, 891-904.
- P. Mercelis, J. K. (2006). Residual stresses in selective laser sintering and selective laser melting. *Rapid Prototyping Journal*, 12, 254-256.
- Q. Yan, B. S. (2020). Comparative study of performance comparison of AlSi10Mg alloy prepared by selective laser melting and casting. *Journal of Materials Science & Technology*, 41, 199-208.
- R. Casati, M. H. (2018). Effects of Platform Pre-Heating and Thermal-Treatment Strategies on Properties of AlSi10Mg Alloy Processed by Selective Laser Melting. *Metals*, 8, 954.
- R.J. Moat, A. P. (2011). Residual stresses in laser direct metal deposited Waspaloy. *Materials Science and Engineering: A*, 528, 2288-2298.
- S. Marola, S. B. (2021). Residual stresses in additively manufactured AlSi10Mg: Raman spectroscopy and X-ray diffraction analysis. *Materials & Design*, 202, 109550.
- T. DebRoy, H. W.-H. (2018). Additive manufacturing of metallic components – Process, structure and properties. *Progress in Materials Science*, 92, 112–224.
- T. Thiede, S. C. (2018). Residual Stress in Selective Laser Melted Inconel 718: Influence of the Removal from Base Plate and Deposition Hatch Length. *Materials Performance and Characterization*, 7, 717-735.
- X.X. Zhang, A. L. (2021). Evolution of microscopic strains, stresses, and dislocation density during in-situ tensile loading of additively manufactured AlSi10Mg alloy. *International Journal of Plasticity*, 139, 102946.

Z. Wang., E. D. (2017). Residual stress mapping in Inconel 625 fabricated through additive manufacturing: Method for neutron diffraction measurements to validate thermomechanical model predictions. *Materials & Design*, 113, 169-177.